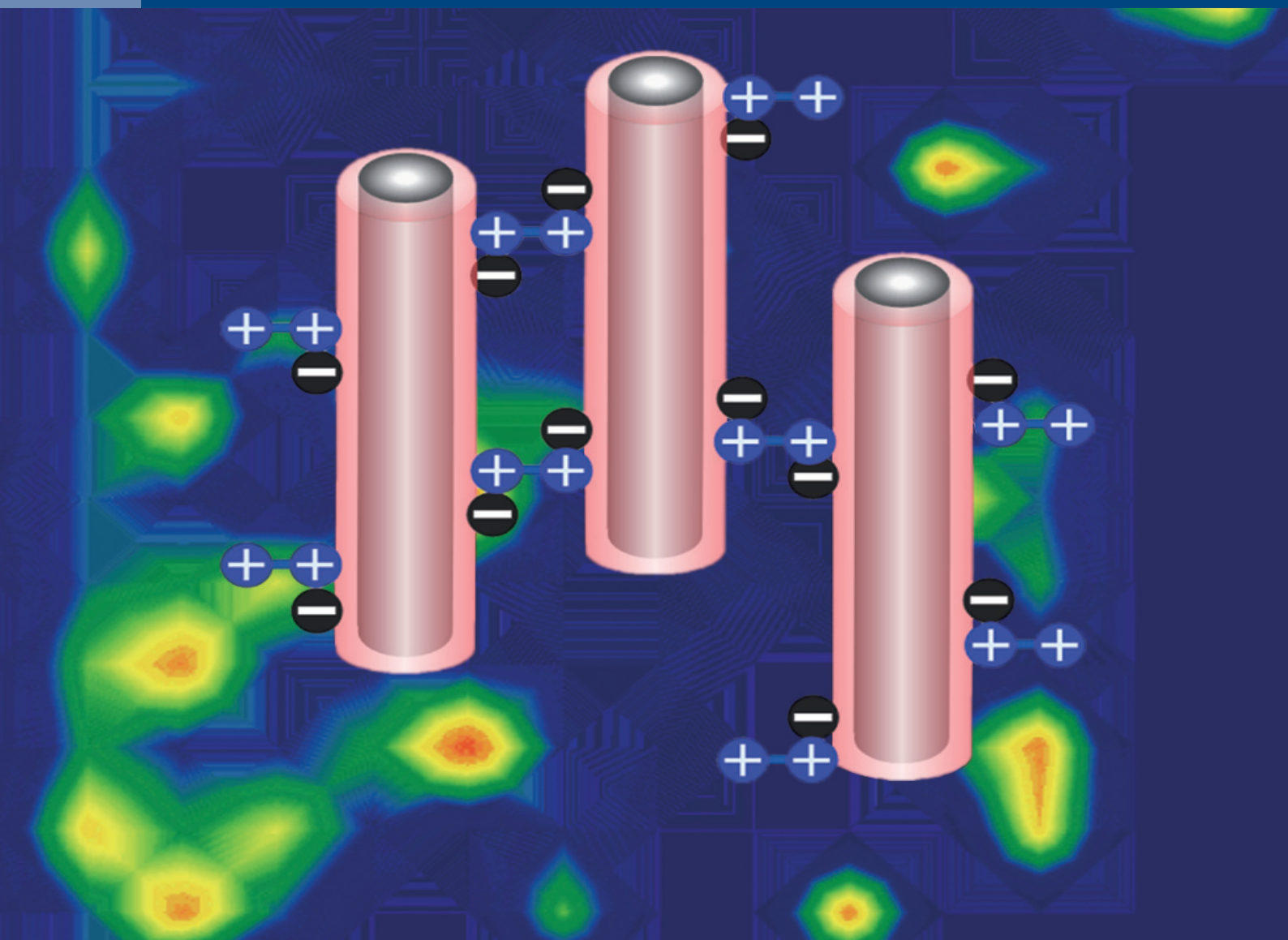JSS

JOURNAL OF
SEPARATION
SCIENCE

22|18

Methods
Chromatography · Electroseparation

Applications
Biomedicine · Foods · Environment

www.jss-journal.com

WILEY-VCH

JOURNAL OF
SEPARATION SCIENCE

Antibody adsorption in protein-A affinity chromatography – in situ measurement of nanoscale structure by small-angle X-ray scattering

Jacek Plewka[1,3] (iD) | Gonçalo L. Silva[3,4,5] | Rupert Tscheließnig[2,3] | Harald Rennhofer[1] (iD) | Cristina Dias-Cabral[4,5] (iD) | Alois Jungbauer[2,3] (iD) | Helga C. Lichtenegger[1] (iD)

[1]Department of Material Science and Process Engineering, University of Natural Resources and LifeSciences, Vienna, Austria

[2]Department of Biotechnology, University of Natural Resources and Life Sciences, Vienna, Austria

[3]Austrian Centre of Industrial Biotechnology, Vienna, Austria

[4]CICS-UBI – Health Sciences Research Centre, University of Beira Interior, Covilhã, Portugal

[5]Department of Chemistry, University of Beira Interior, Covilhã, Portugal

Correspondence
Professor Helga Lichtenegger, Institute of Physics and Materials Science (IPM) Peter-Jordan-Straße 82, 1190 Vienna, Austria.
Email: helga.lichtenegger@boku.ac.at

Protein-A chromatography is the most widely used chromatography step in downstream processing of antibodies. A deeper understanding of the influence of the surface topology on a molecular/nanoscale level on adsorption is essential for further improvement. It is not clear if the binding is homogenous throughout the entire bead network. We followed the protein absorption process and observed the formation of a protein layer on fibers of chromatography resin in a time-resolved manner in nanoscale. To characterize the changes in the antibody-protein-A ligand complex, small angle X-ray scattering was employed using a miniaturized X-ray-transparent chromatography column packed with a MabSelect SuRe resin. Antibody-free MabSelect SuRe resin fiber had an average radius of 12 nm and the protein layer thickness resulting from antibody adsorption was 5.5 and 10.4 nm for fiber and junctions, respectively under applied native conditions. We hypothesize that an average of 1.2 antibodies were adsorbed per protein-A ligand tetramer bound to the outermost units. In contrast to previous studies, it was therefore possible for the first time to directly correlate the nanostructure changes inside the column, which is otherwise a black box, with the adsorption and elution process.

KEYWORDS
agarose, immunoglobulin, protein layer thickness, protein-A chromatography, small angle X-ray scattering

1 | INTRODUCTION

Although protein-A affinity chromatography is the most commonly employed method for the purification of antibodies, the adsorption process on the nanoscale is yet not well understood. Previous models rely on the crystal structure of the protein-antibody complex [1–4], or the amount of adsorbed antibody from bulk solution [5]. However, direct information about the structural changes inside the column during the adsorption process requires a method capable of following the process in situ and on the nanoscale length. This is a challenging task, since the investigation has to be performed in a time resolved way and under native process conditions. Despite great progress in understanding the nature of interactions between antibody and affinity resins during the purification step, previous investigations heavily depended on

empirical methods such as comparison of the sensors signals before and after chromatography column [6–9]. This leaves the structural changes inside the chromatography column, where the actual process happens which is unclear, thus creating "missing link".

Full-length protein-A from *Staphylococcus aureus* is composed of five homologous binding domains [10]; however, to improve its selectivity and alkaline stability, protein-A ligands used in chromatography are made from engineered domains (most popularly derived from the B-domains or the C-domain) [11] immobilized on chromatographic supports, such as agarose or hydroxylated methacrylic polymer [12].

Protein layer thickness refers to the amount of protein adsorbed at a solid surface and it's positioning towards it, and has been the subject of numerous studies in the last five decades [13,14]. However, for more complex systems, such as protein-A chromatography resin, in which antibody is adsorbed to the surface via ligand-mediated interactions, the applicable research methods are greatly limited. Mazzer et al. [15] proposed neutron reflectivity measurements to probe the protein-A–antibody complex arrangement at the solid-liquid interface. However, they immobilized protein-A ligands on the silicon surface, compromising the native state of the chromatography bead backbone and performed the experiment in batch mode. Also other methods used for the structural determination of protein-surface interactions require a sample pretreatment resulting in non-native process conditions as described in the review by Rabe et al. [16].

In the present study, we followed antibody layer formation in situ and their adsorption and desorption kinetics on a protein-A chromatography resin during a typical purification run. We used MabSelect SuRe (GE Healthcare), a popular protein-A chromatography resin, as the model system and small angle X-ray scattering (SAXS) as the probing method. Cross-linked, porous agarose beads 85 µm in diameter are characterized by a rigid, high-flow backbone matrix and a tetrameric ligand of synthetically engineered B-domains, called Z-domain, immobilized via short linkers [16,17]. From equilibrium binding capacity and ligand density it was derived that on average 3.3 antibody molecules are bound to one MabSelect SuRe protein-A ligand [5,18].

SAXS is a powerful technique for probing the structural properties of materials on the nanoscale and ideally suitable for non-destructive in-solution experiments. The technique is based on elastic scattering of X-ray photons by electrons, which provides information about fluctuations in electron density within illuminated sample volumes. The use of brilliant synchrotron radiation facilities allows time-resolved studies on versatile materials, making it an excellent tool for investigating the development of protein layer thickness and its kinetics under native chromatography conditions [19].

SAXS is routinely applied to study conformational changes to the proteins directly after elution from the column in HPLC–SAXS modes [20] like HIC–SAXS [21], SEC–SAXS [22,23] as well as to study structure of porous materials often with the combination of other structural characterization methods like SEM [24]. However, the method to follow the adsorption process in situ in the column by SAXS opens up a new avenue to deeper investigation of all modes of chromatography.

2 | Materials and methods

2.1 | Materials

For protein-A chromatography, an agarose-based resin (MabSelect™ SuRe™, GE Healthcare) was used. The model protein used for this investigation was 13 mg/mL Herceptin® (Trastuzumab–humanized IgG1) solution from Roche dialyzed into running buffer (0.01 mM phosphate buffer with 150 mM NaCl, pH 7.4). The quality of the antibody solution was assessed on SEC column (Supporting Information Figure S1). No dimerization of protein solution was observed. Sodium phosphate dibasic, sodium dihydrogen phosphate, sodium chloride, and glycine-HCl were purchased from Merck Millipore.

2.2 | Chromatography column for in situ SAXS

A miniature chromatography column was built in our laboratory for simultaneous chromatography runs and in situ characterization by SAXS (Figure 1). The column resembled a conventional HPLC column, a cylinder filled with a stationary phase closed with a frit at the bottom. A capillary (Hilgenberg–mark tube from quartz glass) with 1.5 mm diameter and 10-µm thick glass walls to reduce the absorbance of X-rays was glued into a metal housing for protection. A gap in the metal housing allowed undisturbed passing of photons. The SAXS column was connected to an ÄKTAprime plus chromatography system via HPLC connectors for flow-through experiments and placed in the incident X-ray beam for in situ measurements. A 280 nm UV signal was collected downstream of the column. The resulting UV chromatographs were time-corrected based on the additional volume between the column and UV sensor.

2.3 | Protein-A chromatography run

The chromatography run included equilibration of the SAXS column with running buffer (0.01 mM phosphate buffer with 150 mM NaCl, pH 7.4), injection of 4 mg of monoclonal antibody standard solution from the loop to oversaturate the column, washing off unbound free antibodies, and a subsequent elution step with 0.1 M glycine buffer (pH 3.5). A constant flow rate of 0.1 mL/min was applied throughout

chromatography run. Both conductivity and UV 280 nm signal were collected (Supporting Information Table S1).

2.4 | In situ X-ray characterization

In situ on-line characterization of the protein-A chromatography process by SAXS was performed at the European Synchrotron (ESRF, Grenoble, France), beamlines BM26B [25], and BM29 [26]. Scattering images with an exposure of 1 s were collected every second throughout the protein-A chromatography purification process using a 2D detector (Pilatus 1 M) at a photon energy of 12 keV ($\lambda = 1.033$ Å) and sample to detector distance of 5 m. The 2D images were further processed using an ESRF integrated data reduction system to obtain plots of the intensity dependence on scattering vector q, defined as $q = 4\pi \sin(\theta)/\lambda$, where 2θ is the scattering angle. The q range used for data evaluation was trimmed to 0.03 to 1.83 nm^{-1} to exclude noisy data. Subsequent data processing and model fitting was performed in Mathematica 11.2 [27]. Measurements were repeated several times to ensure reliable results, in particular since the signal from the resin was superimposed on the signal from the protein layer. The same data features were reproducibly found throughout all scattering measurements, thus allowing the extraction of subtle changes. From all measurements performed, only one typical set is presented in this manuscript. Results from multiple experiments are available in the Supporting Information Figure S2.
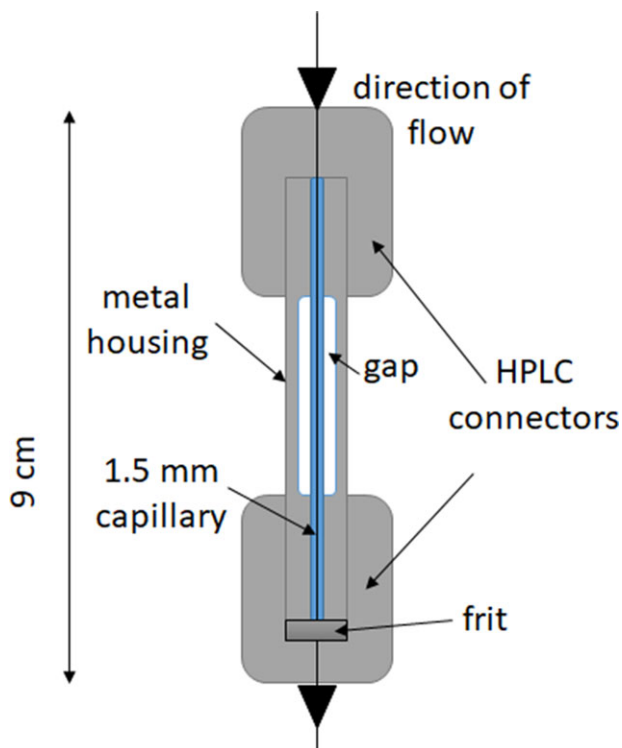

**FIGURE 1** Schematic of a SAXS column

2.5 | SEM of agarose

In order to visualize the inner structure of the agarose network in MabSelect SuRe resin, a modified drying protocol was applied [28]. Agarose beads were transferred into 2.3 M sucrose solution, which worked as a cryoprotectant, and flash-frozen using liquid nitrogen. A solid bead drop was then cut using an MT-990 Motorized Precision Microtome from RMC Boeckeler equipped with a tungsten carbide knife. The 30-μm-thick bead slices were collected and dehydrated in graded ethanol series prior to drying with CO_2 solution using a Critical Point Dryer Leica EM CPD030. The resulting dried agarose bead slices were transferred to an aluminum slab and sputter coated with an Au layer approximately 4 nm thick prior to visualization using the Scanning Electron Microscope Quanta^{TM} 250 FEG from FEI under high vacuum conditions.

3 | RESULTS AND DISCUSSION

3.1 | Protein-A chromatography and in situ SAXS

Protein-A chromatography was performed with a miniature column built in our laboratory for simultaneous chromatography runs and in situ characterization by SAXS. A flow experiment was chosen over regular batch study, as it ensures a constant amount of resin within the illuminated volume of X-ray beam throughout the chromatography run. Such approach guarantees that the observed changes in the scattering profiles are exclusively caused by introduced protein or its interactions with chromatography resin. Moreover, flow experiments allow studying not only adsorption phenomenon like in batch mode, but also the desorption strengthening our understanding of the whole process. Scattering profiles representing structural changes inside the chromatography column were recorded every second in situ throughout the protein-A chromatography run using SAXS. The product was characterized by a UV sensor further downstream in order to correlate the chromatogram with the SAXS results. To ensure protein saturation of the resin binding sites within the SAXS column, the capacity of the resin at given conditions and flow rate was exceeded, which was represented as a sharp peak in the UV data phase called "wash" (Figure 2A). Note that the amount of protein absorption achieved in this way may be different from the maximal possible amount that is calculated from the isotherm at equilibrium conditions, but corresponds to the maximum under the given circumstances, as it would occur in an industrial process. Free, unbound antibodies present in the column were washed off using running buffer to ensure that only bound protein and the resin contributed to the scattering profile at this stage of the protein-A run. Elution of the bound
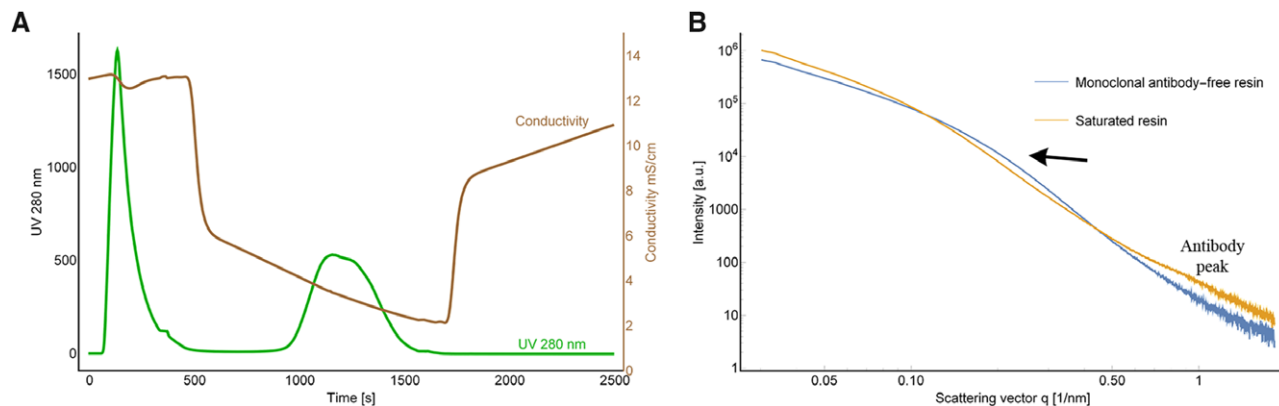
FIGURE 2 (A) Chromatograph of the 280 nm UV signal (green) and conductivity (brown) for the protein-A run. (B) Scattering profiles for antibody-free MabSelect SuRe resin (blue) and saturated resin (orange). The transition of the shoulder visible at $q = 0.2$ nm^{-1} for antibody-free resin to saturated resin is highlighted by the arrow. Additionally, regions for dimensionality and Porod fits are indicated

protein from the protein-A resin was achieved by lowering the pH on the column to disrupt the affinity of antibodies towards protein-A ligands.

In Figure 2B, representative SAXS curves (the same for multiple performed experiments) are shown for the antibody-free MabSelect SuRe taken from the "injection" or "regeneration" phase and the corresponding saturated resin from the "wash" and "elution" phases before the elution peak. The shoulder present at $q = 0.2$ nm^{-1} representing resin feature (blue curve) clearly moves to a smaller q during saturation (orange curve), indicating an increase in the analyzed system size according to the reciprocal nature of Bragg's law. Furthermore, the intensity at the higher q ($q = 0.6$ nm^{-1}) becomes stronger during protein loading. Antibodies have a radius of gyration of roughly 5 nm [29], which leads to a SAXS signal in this region. Therefore, we attribute this part of the SAXS curve to the presence of antibodies and denote it in the figure as an antibody peak. In contrast, the shoulder at the lower q is also present without protein and attributed to the resin (with and without bound protein).

3.2 | SAXS parameters reflecting protein adsorption

In addition to the qualitative changes in the SAXS curve upon protein adsorption and elution, quantitative parameters have to be extracted from different parts of the SAXS curve to follow the structural changes during purification.

3.2.1 | Dimensionality

At very low q, decay of the SAXS curve is given by the dimensionality of the scatterer: $I(q) \sim q^{-D}$, where D corresponds to 0 for spheres, 1 for rod-like scatterers, and 2 for plate-like scatterers. In a double logarithmic plot, D is given by the slope of the curve (Figure 2B). The slope changes from 1.6

in the antibody-free resin to 2 in the saturated resin, which corresponds to a change from slender to thicker fibers and is in good agreement with the actual structure of MabSelect SuRe.

3.2.2 | Correlation length estimate

The parameter that qualitatively describes structural changes as an estimate of the intensity-averaged electron density fluctuations throughout illuminated sample volume is l_{CH}^* (Eq. (1))

$$l_{CH}^* = \frac{\pi}{Q} \cdot \int_{q_{min}}^{q_{max}} I(q) \cdot q \cdot dq$$

$$\text{where } Q = \int_{q_{min}}^{q_{max}} I(q) \cdot q^2 \cdot dq \qquad (1)$$

where l_{CH}^* is the mean correlation length estimate and Q is the invariant.

Unlike the radius of gyration determination, which requires fitting according to Guinier's approximation, the correlation length is calculated based on the integral of the scattering profile and thus is less sensitive to noisy data [30,31]. Moreover, in contrast to the Guinier approximation, evaluation of the correlation length does not require the sample to be dilute.

3.2.3 | Fractal dimension and surface roughness

The higher q portion of the scattering curve ($qR >> 1$) is generally determined by Porod's law, according to which the scattered X-ray intensity decreases with q^{-4} for smooth 3D objects, but the exponent can also deviate from 4 in the case of a volume or surface fractal. The antibody-free resin has an exponent close to 4, which then approaches 3.5 during protein adsorption. Surface fractals have values between 3 and 4, which clearly indicate increased surface roughness. The q
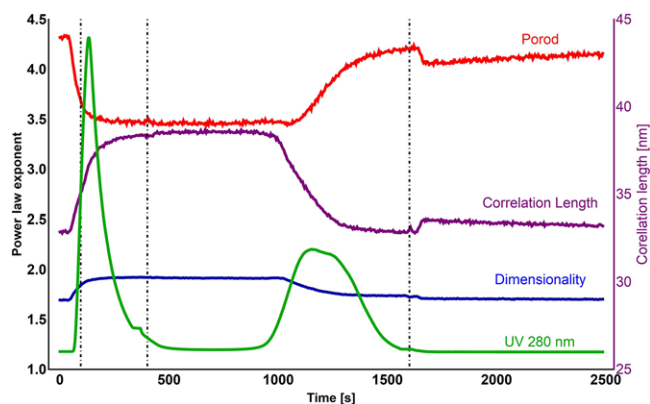
FIGURE 3 Comparison of overall fitting parameters for the SAXS time series overlaid on top of the UV signal

region used for Porod fitting is shown in Supporting Information Figure S3.

3.3 | Time evolution of SAXS parameters

All of the above SAXS parameters were quantitatively evaluated at each time point during a protein-A chromatography run using Mathematica software [27] and could be exactly correlated with the purification steps by simultaneous UV analysis (Figure 3). Both SAXS parameters and UV signal clearly responded to the process of loading antibody solution on the column and reached a plateau as soon as the resin was saturated. Since the amount of the chromatographic resin within a column is constant in time, all the changes in fitted SAXS parameters have to be caused by loaded and discharged protein solution or its interactions with the resin. This assumption is also validated by the fact that all of mentioned parameters come back to their initial values after the protein elution.

The saturated resin SAXS signal after the "wash" phase is characterized by plumper resin fibers (higher dimensionality) with longer correlation length (larger l_{CH}^*). Notably, the dimensionality and correlation length, although extracted from different features of the SAXS curve, proceed in parallel throughout the chromatography process, confirming the evolution from slender to plumper fibers via adsorption of protein. Therefore, the development of l_{CH}^* is attributed to the presence of an antibody layer on top of the chromatographic resin.

The fractal dimension sharply decreases after injection, which corresponds to an increasing surface roughness in the saturated resin, and reaches a plateau in parallel with the other parameters. After elution of the bound antibodies from the SAXS column, all parameters gradually returned to their initial values. The final scattering profile after regeneration of the MabSelect SuRe resin with the running buffer resulted in a signal identical to the initial signal ($\chi^2 = 0.01$),

indicating that the system fully recovered and was ready for the next chromatographic run.

Therefore, we have shown with a simple fitting routine that we can follow the protein-A purification process in situ using SAXS as a probing method. Moreover, the method allowed us to identify and initially characterize structural changes in the system due to adsorption and also desorption phenomena using the "model-free" approach that is independent of the detailed structure of the analyzed system and requires no data modeling.

Note that due to the relatively low concentration of monoclonal antibodies in the bulk solution (and the low X-ray contrast of protein with respect to water), the main signal comes from the resin in the beam and the monoclonal antibodies tightly packed to it. It contributes to the scattering profiles so much that it completely overshines the signal from the freely floating monoclonal antibodies (see also Supporting Information Figure S4).

3.4 | Protein layer thickness

As the analysis of general SAXS parameters allows us to follow adsorption processes in a time-resolved manner by applying a simple fitting routine, quantitative information on layer thickness and its development depend on the resin structure and, therefore, requires the use of a structural model. Thus, we studied the morphology of the virgin resin using SEM. Images were recorded on cryo-cut beads clearly showing the agarose internal network (Figure 4A).

3.4.1 | Structural analysis of resin

For further analysis, a semi-automated algorithm for SEM image processing was applied to obtain a general overview of size distribution within the internal structure of the Mab-Select SuRe agarose network. First, the SEM image from MabSelect SuRe was binarized and processed (erosion, Gaussian filters) to visualize the strands and junctions in the first plane of the picture. Next, circles were automatically assigned for the binarized features with diameters corresponding to the locally longest Euclidean distances between "no data" points. The histogram of all radii within an analyzed image (Figure 4B) represents the normalized distribution of all feature radii between 3 and 70 nm (1 nm bin width). Roughly two populations were identified: the peak at ~11 nm attributed to the mean fiber thickness, and the broader peak centered at ~30 nm attributed to junctions between strands. The results are biased by the applied analytical method and some of the values may be overpopulated due to the irregularity in their shape.
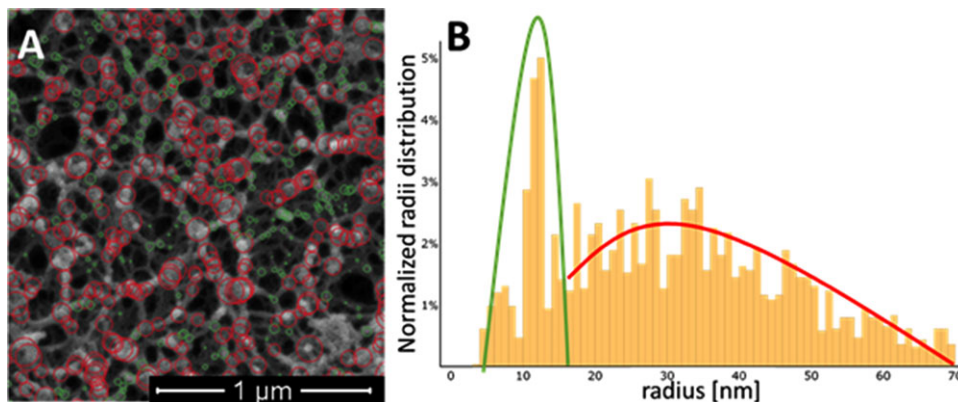
FIGURE 4 (A) An overlay of Euclidean circles representing the feature diameters within the first plane of the MabSelect SuRe internal agarose network over a SEM picture. Green circles represent radii between 3 and 15 nm, red circles represent radii of 15 to 70 nm. (B) A histogram of normalized radii distribution from the semi-automated feature detection algorithm. Green peak is attributed mean fiber thickness, the red peak to junctions between strands
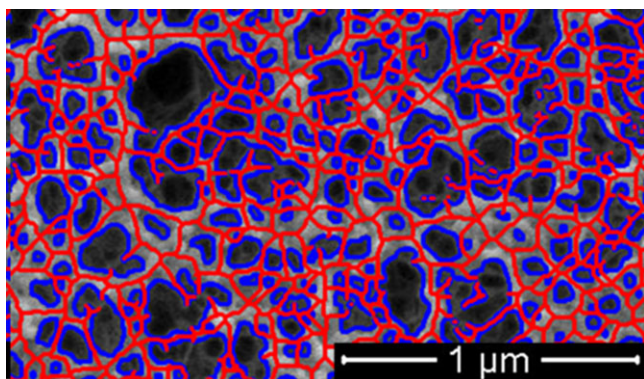
FIGURE 5 Visual representation of the broken rod model for an agarose network with infinitely long fibers cross-linked to create junctions. Red, center of agarose fibers in the first plane; blue, edges of fibers

3.4.2 | Broken rod model

The internal structure of the MabSelect SuRe agarose backbone can be approximated by the so-called broken rod model [32] based on a system consisting of long agarose fibers approximated with infinitely long cylinders characterized by the cross-sectional radius R_1 and cross-linked junctions with radius R_2 (Figure 5). The scattered intensity is then given by $I(q)$ (Eq. (2)).

$$I(q) \sim \sum_{i=1}^{2} k_i/q \left[\frac{J_1(qR_i)}{qR_i} \right]^2 \quad (2)$$

Where k_i denotes the relative weights of cylinder radii R_1 and R_2, and $J_1(x)$ is the Bessel function of the first kind for infinitely long cylinders ($L >> R$). Assuming a distribution of R_1 and R_2 about a mean value, we obtain Eq. (3).

$$I(q) \sim \sum_{i=1}^{2} k_i/q \int_0^\infty \left[\frac{J_1(qx)}{qx} \right]^2 \cdot G(x)_i dx \quad (3)$$

Where $G(x)$ is the normal distribution of each radius separately as determined in Eq. (4):

$$G(x)_i = \frac{1}{\sqrt{2\pi\sigma_i^2}} \cdot e^{-\frac{(x-\mu_i)^2}{2\sigma_i^2}} \quad (4)$$

Where μ_i is the mean of the distribution and σ_i^2 is the variance.

Although the broken rod model is certainly idealized, it has already been applied successfully to analyze the gelation process of polysaccharide gels, such as alginate [33–35] or sorbitol [36], to obtain insight into the kinetics of gel formation and structural information about fiber diameter throughout the process. The model assumes that infinitely long agarose strands of characteristic diameter are interconnected, creating nodes of different thickness denoted as junctions and, therefore, approximated as two populations of rigid cylinders (Figure 5). Similar models built on polydisperse cylinders were also used for other agarose-based chromatographic materials characterization using small angle neutron scattering [37]. The broken rod model, however, demonstrated a superior fit to experimental data (Figure 6A) (a comparison to other models is shown in the Supporting Information Table S2 and Figure S5).

3.4.3 | Protein layer thickness

The broken rod model was used to quantitatively evaluate the evolution of resin strand and junction thickness during adsorption and desorption in the chromatography run. According
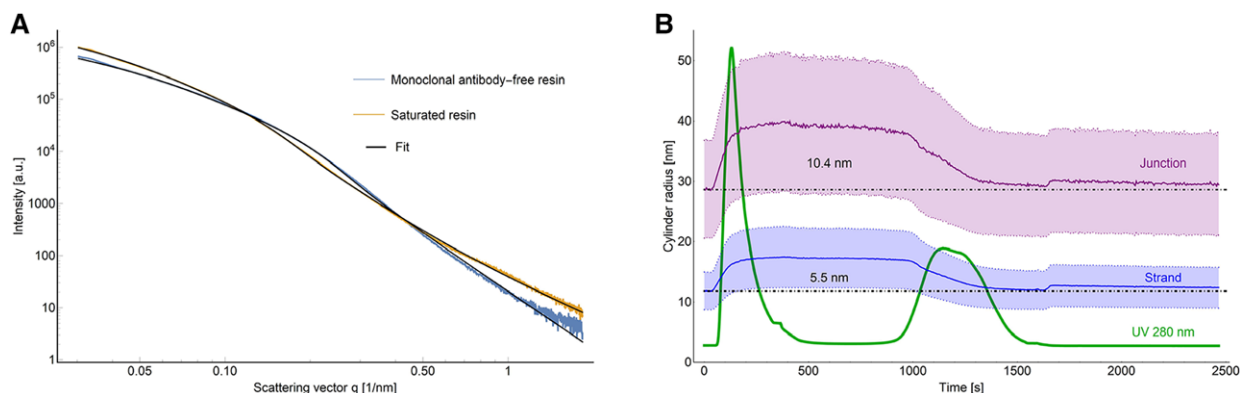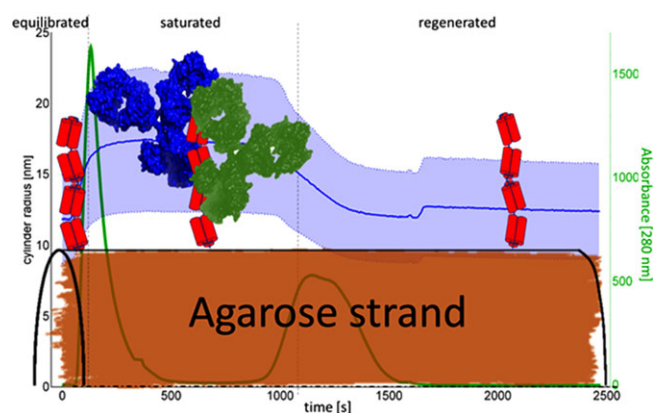
FIGURE 6 (A) Fit of broken rod model (black) to corresponding scattering profiles. Due to good agreement between data and fit it lays directly on top of the data points. (B) Evolution of the radii of strands (blue) and junctions (purple) with their corresponding size distribution during a protein-A chromatography run

TABLE 1 Comparison of the radii of strands and junctions according to the broken rod model and resulting protein layer thickness

	Strand radius ± distribution, nm	Junction radius ± distribution, nm
Antibody-free resin	11.8 ± 3.1	28.7 ± 8.1
Saturated MabSelect SuRe resin	17.3 ± 5.0	39.1 ± 11.2
Resulting protein layer thickness	5.5 ± 5.9	10.4 ± 13.8

FIGURE 7 Structural interpretation of protein layer thickness development throughout the protein-A chromatography run. Protein-A ligand tetramers (in red) are attached to the agarose strand (orange). All entities are in scale to facilitate size comparison

to the broken rod model, the antibody-free MabSelect SuRe resin is characterized by an average cylinder radius of 11.8 and 28.6 nm for agarose strands and junctions, respectively for all performed measurements, which is in a good agreement with both the literature [28] and visual examination of SEM micrographs (Figure 4A). Upon saturation of the chromatographic resin with an antibody solution, as indicated by the first peak in the UV spectrum (Figure 2A), the agarose strand radius increased 250 s after the protein injection, and then plateaued until protein elution. The difference in the values between antibody-free and saturated agarose strands of 5.5 nm (Table 1) was attributed to so-called protein layer thickness, an important mechanistic parameter that could potentially indicate a change in the conformation of the adsorbed protein or in the protein orientation within the layer. The resulting protein layer thickness for junctions was calculated as being almost twice as long. The difference in protein layer thickness for strands and junctions could be explained by a steric hindrance effect in which cross-linked strands block certain positions of the antibody-protein-A complex, promoting antibody binding to protein-A ligand units further away from the surface of junctions. As presented in Figure 6B, values for the strand and junction radii gradually return to their initial values due to subsequent elution steps. Therefore, performing measurements in flow instead of batch mode, we not only

assessed native process conditions, but also examined both adsorption and desorption structural changes on nanometer scale.

The broken rod model readily provides insight into the protein layer thickness and its kinetics in the MabSelect SuRe resin system. The model also allows speculation about the structural changes within a very complex system. We suggest the following structural interpretation of the protein layer thickness results (Figure 7). Agarose strands (11 nm mean radius) are grafted with protein-A tetramer ligands, which have a length of approximately 10 nm when stretched (single unit of *Staphylococcus aureus* protein-A has a length of 3 nm, Protein Data Bank:1BDD [38]). According to the broken rod model, the radius of antibody-free MabSelect SuRe strands is 11.8 ± 3.1 nm; thus, protein-A ligands contribute only slightly, if at all, to the strand thickness derived from the SAXS scattering profile. A possible explanation would be a

relatively low spatial grafting density of protein-A ligands on top of the agarose strand surface. Moreover, a high degree of ligand flexibility can smear the protein-A contribution to the resulting SAXS scattering profiles. When saturated, the MabSelect SuRe strand radius increases to 17.3 ± 5.0 nm. The resulting protein layer thickness is caused by the attachment of antibody moieties to protein-A ligand units via Fc-mediated binding, which stiffens their structure. Knowing the amount of protein adsorbed (the elution peak area from the chromatograph), the binding capacity is calculated to be ∼35 mg of antibodies per milliliter of MabSelect SuRe resin. Taking into account molecular weights of 150 and 26.7 kDa for monoclonal antibody and protein-A ligand, respectively, we estimate 1.2 molecules of antibodies bound to each protein-A ligand tetramer (taking 5.6 mg of protein-A ligand per milliliter of MabSelect SuRe resin) [39,40]. Therefore, we conclude that there are ten possible binding configurations for one or two antibodies in complex with protein-A ligand, which explains the slightly greater distribution of sizes for agarose strands when saturated with antibodies. The resulting protein layer thickness of 5.5 ± 5.9 nm is well below the average diameter of IgG1 protein (11.5 nm, Protein Data Bank: 1HZH) [41].

The distribution indicates that there are places on agarose strands at which no protein is present, up to a protein layer thickness of approximately 12 nm, matching the width of IgG. Potentially, the above consideration would suggest that antibodies are positioned in proximity to and facing the agarose fiber surface, so that we are probing the thickness and not the length of the antibody. However, the significant size distribution of protein layer thickness derived from the additive nature of combining distributions $((\sigma_z)^2 = (\sigma_1)^2 + (\sigma_2)^2)$ would also allow other configurations with antibodies positioned side-on close to the surface, but tilted, though there is a lower probability of their occurrence. To position antibody parallel to an agarose strand in proximity of the surface, the antibody-protein-A complex has to possess high bending and rotation freedom, which would only be possible if the antibody is bound to the outermost units of a protein-A ligand tetramer. Similar observations were made using neutron reflectivity to measure protein-A-antibody complex distance on a silica surface [15]; Mezzer et al. suggested that two IgG molecules are bound to a protein-A tetramer ligand with "a somewhat skewed orientation and close proximity to the silica surface". They also concluded that antibody was bound to the protein-A ligand tetramer domain in a side-on to tilted orientation further from the silica interface. Having similar conclusions to ours, the work of Mezzer et al. strengthens our reasoning, especially as they worked in the idealized and therefore easier to characterize environment in batch mode with protein-A ligands immobilized on silicon wafer instead of native chromatography resin under flow conditions.

The nature of junctions is harder to decipher, as they are less consistent in shape and size and we do not know if the protein-A ligand grafting density is the same as for strands. Thus, junctions have a considerable size distribution of 28.7 ± 8.1 nm, which is even higher when junction ligands are saturated with antibodies (39.1 ± 11.2 nm). Therefore, the protein layer thickness for a junction is 10.4 ± 13.8 nm, approximately twice as thick as strands. The above data are suggestive of a different profile of the antibody-protein-A ligand complex structure for many ligands available on the surface of junctions compared to those on strands. Some of the ligand units may not be available for antibody binding due to a steric hindrance effect of cross-linking strands blocking likely more energetically favorable binding sites, which would explain different sizes and the substantial size distribution of junction protein layer thickness.

A SAXS investigation on the similar agarose-based chromatography resin was reported by Koshari et al. [38], where they investigated among others SP Sepharose FF resin using neutrons. SP Sepharose FF is a cation exchanger resin based on 4% cross-linked agarose like the backbone of MabSelect SuRe resin, therefore one would expect similar scattering profiles and subsequent structural parameters for both of them. However, both the applied methodology and results show significant discrepancies between our work and Koshari's. Koshari used polydisperse cylinder model resulting in mean cylinder radii of around 1 nm reasoning it to be a rigid single or double helices from agarose within strand, whereas with the broken rod model we obtained a strand radius of almost 12 nm, which is in hand with literature and SEM investigation. Moreover, within the broken rod model we assumed not only infinitely long cylinders instead of artificially setting them to 1000 nm in length, but also used two populations of cylinders to account for junctions which played important role in the architecture of cross-linked agarose beads. This resulted in a better fit of the model to the data as visually compared to fits reported in Koshari's paper and more consistent results of strands and junctions' radii. It should be noted, however, that Koshari et al. did their study with SANS, while ours was performed with SAXS; therefore, the different size of the observed resin fibrils/strands might be due to the different contrast for neutrons and X-rays, in particular since they used D_2O as a solvent, thus potentially enhancing the contrast between individual fibrils (single or double helices) within a single resin strand.

Irrespective of the applied model, the agarose network with its stands and junctions exhibit a quite distinctive surface topology with two different adsorption sites showing layers of different thickness. The developed methodology could be applied to any other chromatography method such as IEC, hydrophobic interaction or multimodal chromatography with stationary phase based on agarose backbone.

4 | CONCLUDING REMARKS

Using a simple fitting routine without any further modeling can follow the structural changes occurring in situ in a miniaturized chromatography column. An entire chromatography run from equilibration, through loading and washing, to elution can be observed in situ under native conditions using SAXS as a probing method. Moreover, based on the SEM micrographs, we created a model allowing us to characterize the internal structure of the MabSelect SuRe agarose network with infinitely long cross-linked cylinders of characteristic thickness representing strands and junctions within the system. We monitored the development of the radii of these cylinders throughout a protein-A chromatography run and found that the agarose strands have an average radius of 11.8 nm, while upon saturation with antibodies the difference was identified as the protein layer thickness (5.5 and 10.4 nm for strands and junctions, respectively). Based on the information on the system's components and parameters, we hypothesize that an average 1.2 antibodies are bound to each protein-A ligand tetramer. Most likely, they are bound to the outermost units within tetramer ligands from the agarose surface and the whole complex is parallel to the surface in its proximity, where we probed the antibody thickness in side-on or tilted orientation.

CONFLICT OF INTEREST

The authors have declared no conflict of interest.

ORCID

Jacek Plewka http://orcid.org/0000-0002-0307-0907
Harald Rennhofer http://orcid.org/0000-0003-0743-316X
Cristina Dias-Cabral
http://orcid.org/0000-0002-2759-7762
Alois Jungbauer http://orcid.org/0000-0001-8182-7728
Helga C. Lichtenegger
http://orcid.org/0000-0002-6624-1419

REFERENCES

1. Deisenhofer, J., Crystallographic refinement and atomic models of a human Fc fragment and its complex with fragment B of protein A from Staphylococcus aureus at 2.9- and 2.8-A resolution. *Biochemistry* 1981, *20*, 2361–2370.

2. Graille, M., Stura, E. A., Corper, A. L., Sutton, B. J., Taussig, M. J., Charbonnier, J. B., Silverman, G. J., Crystal structure of a Staphylococcus aureus protein a domain complexed with the fab fragment of a human IgM antibody: structural basis for recognition of B-cell receptors and superantigen activity. *Proc Natl Acad Sci U S A* 2000, *97*, 5399–5404.

3. Deis, L. N., Wu, Q., Wang, Y., Qi, Y., Daniels, K. G., Zhou, P., Oas, T. G., Suppression of conformational heterogeneity at a protein-protein interface. *Proc Natl Acad Sci U S A* 2015, *112*, 9028–9033.

4. Sauer-Eriksson, A. E., Kleywegt, G. J., Uhlen, M., Jones, T. A., Crystal structure of the C2 fragment of streptococcal protein G in complex with the Fc domain of human IgG. *Structure* 1995, *3*, 265–278.

5. Ghose, S., Hubbard, B., Cramer, S. M., Binding capacity differences for antibodies and fc-fusion proteins on protein a chromatographic materials. *Biotechnol. Bioeng.* 2007, *96*, 768–779.

6. Iyer, H., Tapper, S., Lester, P., Wolk, B., van Reis, R., Use of the steric mass action model in ion-exchange chromatographic process development. *J. Chromatogr.* 1999, *832*, 1–9.

7. Orellana, C. A., Shene, C., Asenjo, J. A., Mathematical modeling of elution curves for a protein mixture in ion exchange chromatography applied to high protein concentration. *Biotechnol. Bioeng.* 2009, *104*, 572–581.

8. Gerontas, S., Shapiro, M. S., Bracewell, D. G., Chromatography modelling to describe protein adsorption at bead level. *J. Chromatogr.* 2013, *1284*, 44–52.

9. Mallik, R., Hage, D. S., Affinity monolith chromatography. *J. Sep. Sci.* 2006, *29*, 1686–1704.

10. Lofdahl, S., Guss, B., Uhlen, M., Philipson, L., Lindberg, M., Gene for staphylococcal protein-A. *Proc Natl Acad Sci U S A* 1983, *80*, 697–701.

11. Muller, E., Vajda, J., Routes to improve binding capacities of affinity resins demonstrated for protein A chromatography. *J. Chromatogr. B* 2016, *1021*, 159–168.

12. Boschetti, E., Jungbauer, A., Separation of Antibodies by Liquid Chromatography, chapter 15. Academic Press, San Diego, CA, USA 2000, *2*, 535–630

13. Rabe, M., Verdes, D., Seeger, S., Understanding protein adsorption phenomena at solid surfaces. *Adv. Colloid Interface Sci.* 2011, *162*, 87–106.

14. Vogler, E. A., Protein adsorption in three dimensions. *Biomaterials* 2012, *33*, 1201–1237.

15. Mazzer, A. R., Clifton, L. A., Perevozchikova, T., Butler, P. D., Roberts, C. J., Bracewell, D. G., Neutron reflectivity measurement of protein A-antibody complex at the solid-liquid interface. *J. Chromatogr.* 2017, *1499*, 118–131.

16. Ghose, S., Zhang, J., Conley, L., Caple, R., Williams, K. P., Cecchini, D., Maximizing binding capacity for protein a chromatography. *Biotechnol. Prog.* 2014, *30*, 1335–1340.

17. https://www.gelifesciences.com/en/us/shop/chromatography/resins/affinity-antibody/mabselect-sure-antibody-purification-resin-p-00700?current=17543803 (last time accessed: September 7, 2018).

18. Jungbauer, A., Hahn, R., Engineering protein A affinity chromatography. *Curr Opin Drug Discov Devel* 2004, *7*, 248–256.

19. Blanchet, C. E., Svergun, D. I., Small-angle X-ray scattering on biological macromolecules and nanocomposites in solution, *Annu Rev Phys Chem.* 2013, 37–54.

20. Brookes, E., Perez, J., Cardinali, B., Profumo, A., Vachette, P., Rocco, M., Fibrinogen species as resolved by HPLC-SAXS data processing within the UltraScan Solution Modeler (US-SOMO) enhanced SAS module. *J. Appl. Crystallogr.* 2013, *46*, 1823–1833.

21. Kulsing, C., Komaromy, A. Z., Boysen, R. I., Hearn, M. T., On-line determination by small angle X-ray scattering of the shape of hen egg white lysozyme immediately following elution from a hydrophobic interaction chromatography column. *The Analyst* 2016, *141*, 5810–5814.

22. Ryan, T. M., Trewhella, J., Murphy, J. M., Keown, J. R., Casey, L., Pearce, F. G., Goldstone, D. C., Chen, K., Luo, Z., Kobe, B., McDevitt, C. A., Watkin, S. A., Hawley, A. M., Mudie, S. T., Samardzic Boban, V., Kirby, N., An optimized SEC-SAXS system enabling high X-ray dose for rapid SAXS assessment with correlated UV measurements for biomolecular structure analysis. *J. Appl. Crystallogr.* 2018, *51*, 97–111.

23. O'Brien, D. P., Brier, S., Ladant, D., Durand, D., Chenal, A., Vachette, P., SEC-SAXS and HDX-MS: a powerful combination. The case of the calcium-binding domain of a bacterial toxin. *Biotechnol. Appl. Biochem.* 2018, *65*, 62–68.

24. de Coelho Escobar, C., dos Santos, J. H., Effect of the sol-gel route on the textural characteristics of silica imprinted with Rhodamine B. *J. Sep. Sci* 2014, *37*, 868–875.

25. Portale, G., Cavallo, D., Alfonso, G. C., Hermida-Merino, D., van Drongelen, M., Balzano, L., Peters, G. W. M., Goossens, J. G. P., Bras, W., Polymer crystallization studies under processing-relevant conditions at the SAXS/WAXS dubble beamline at the ESRF. *J. Appl. Crystallogr.* 2013, *46*, 1681–1689.

26. Pernot, P., Round, A., Barrett, R., Antolinos, A. D., Gobbo, A., Gordon, E., Huet, J., Kieffer, J., Lentini, M., Mattenet, M., Morawe, C., Mueller-Dieckmann, C., Ohlsson, S., Schmid, W., Surr, J., Theveneau, P., Zerrad, L., McSweeney, S., Upgraded ESRF BM29 beamline for SAXS on macromolecules in solution. *J. Synchrot. Radiat.* 2013, *20*, 660–664.

27. Wolfram Research, I., Mathematica, Version 11.2 ed., Wolfram Research Inc., Champaign, Illinois 2018

28. Nweke, M. C., Turmaine, M., McCartney, R. G., Bracewell, D. G., Drying techniques for the visualization of agarose-based chromatography media by scanning electron microscopy. *Biotechnol. J.* 2017, *12*, 5.

29. Pilz, I., Schwarz, E., Durchschein, W., Licht, A., Sela, M., Effect of cleaving interchain disulfide bridges on the radius of gyration and maximum length of anti-poly(D-alanyl) antibodies before and after reaction with tetraalanine hapten. *Proc Natl Acad Sci U S A* 1980, *77*, 117–121.

30. Glatter, O., Kratky, O., Small Angle X-Ray Scattering, Academin Press, London 1982

31. Ehmann, H. M. A., Werzer, O., Pachmajer, S., Mohan, T., Amenitsch, H., Resel, R., Kornherr, A., Stana-Kleinschek, K., Kontturi, E., Spirk, S., Surface-sensitive approach to interpreting supramolecular rearrangements in cellulose by synchrotron grazing incidence small-angle X-ray scattering. *Acs Macro Letters* 2015, *4*, 713–716.

32. Guenet, J.-M., Thermoreversible Gelation of Polymers and Biopolymers, Academic Press, London 1992

33. Yuguchi, Y., Hasegawa, A., Padol, A. M., Draget, K. I., Stokke, B. T., Local structure of Ca2+ induced hydrogels of alginate-oligoguluronate blends determined by small-angle-X-ray scattering. *Carbohydr. Polym.* 2016, *152*, 532–540.

34. Yuguchi, Y., Urakawa, H., Kajiwara, K., Draget, K. I., Stokke, B. T., Small-angle X-ray scattering and rheological characterization of alginate gels. 2. Time-resolved studies on ionotropic gels. *J. Mol. Struct.* 2000, *554*, 21–34.

35. Stokke, B. T., Draget, K. I., Smidsrod, O., Yuguchi, Y., Urakawa, H., Kajiwara, K., Small-angle X-ray scattering and rheological characterization of alginate gels. 1. Ca-alginate gels. *Macromolecules* 2000, *33*, 1853–1863.

36. Maeda, H., Yuguchi, Y., Kitamura, S., Urakawa, H., Kajiwara, K., Richtering, W., Fuchs, T., Burchard, W., Structural aspect of gelation in schizophyllan/sorbitol aqueous solution. *Polym. J.* 1999, *31*, 530–534.

37. Koshari, S. H. S., Wagner, N. J., Lenhoff, A. M., Effects of resin architecture and protein size on nanoscale protein distribution in ion-exchange media. *Langmuir* 2018, *34*, 673–684.

38. Gouda, H., Torigoe, H., Saito, A., Sato, M., Arata, Y., Shimada, I., 3-dimensional solution structure of the B-domain of staphylococcal protein-A - comparisons of the solution and crystal-structures. *Biochemistry* 1992, *31*, 9665–9672.

39. Hans, J., Johansson, A. L., Ronnie Palmgren affinity chromatography matrix. 2009.

40. Weinberg, J., Zhang, S., Crews, G., Healy, E., Carta, G., Przyby-cien, T., Polyclonal and monoclonal IgG binding on protein a resins-evidence of competitive binding effects. *Biotechnol Bioeng* 2017, *114*, 1803–1812.

41. Saphire, E. O., Parren, P., Pantophlet, R., Zwick, M. B., Morris, G. M., Rudd, P. M., Dwek, R. A., Stanfield, R. L., Burton, D. R., Wilson, I. A., Crystal structure of a neutralizing human IgG against HIV-1: a template for vaccine design. *Science* 2001, *293*, 1155–1159.

SUPPORTING INFORMATION

Additional supporting information may be found online in the Supporting Information section at the end of the article.